From simple binary to complex multicomponent eutectic alloys

Isaac Chang and Qing Cai

Brunel Centre for Advanced Solidification Technology (BCAST),

Brunel University London, Kingston Lane, Uxbridge, UB8 3PH, UK.

Abstract

The eutectic solidification of almost all binary and majority of key ternary alloy systems have been studied and modelled extensively. The development of eutectic microstructure in ternary, multicomponent and high entropy alloys have generated potential engineering alloys with superior mechanical/magnetic properties that outperform their traditional binary eutectic counterparts due to refined microstructure and/or the presence of dual hard/soft phase mixture. Currently, our understanding of the eutectic solidification is mainly restricted to alloy systems having upto 3 constituents (eg. ternary eutectic). There exists a knowledge gap in our understanding of the solidification behaviour of high order multicomponent eutectic alloys. This review article gives a brief background of the development of eutectic alloys from binary to senary multicomponent systems, together with an overview of recent development of complex microstructures of aluminium based multicomponent alloys with five or more constituents at/near eutectic compositions. Although the number of crystalline phases coexisted in the Al-based eutectic alloys increases with increasing number of

constituents. The solidification of a melt at near eutectic composition of 13-element alloy system has led to the development of seven crystalline phases with predominantly non-cooperative growth, leading to a microstructure free of lamellar feature, as compared to their low-order constituent alloy counterparts. Finally, the hardness of Al-based eutectic alloy increases significantly as the number of constituents in excess of ten. This opens up a new opportunity to develop ultrahigh strength alloys based on high-order multicomponent eutectic alloy systems.

Keywords: Eutectic, multicomponent alloys, microstructure, differential scanning calorimetry, hardness

1. Introduction

Eutectic alloys refer to a unique class of material system comprised of more than one constituent and they exhibit the lowest temperature of melting/freezing as compared to the melting point of any of the constituents. The word eutectic is derived from the Greek word “eutektos” which implies easily melted and it was first used by Guthrie[1] in 1884. Eutectic systems are found everywhere in nature, and have been reported in a wide range of materials including organic[2,3], ceramic[4], metallic[1,5] and semi-metallic[6,7] alloys. They possess a unique composite microstructure of multiple phases, combined with outstanding mechanical and electrical/magnetic properties that exceed their elemental or solid solution counterparts. Our understanding of eutectic materials in terms of their solidification behaviour, crystallographic relationship between eutectic

phases and their properties have been generated through a combination of theoretic and experimental studies for over 130 years. Earlier eutectic alloys were based on low melting point elements[1] including Sn, Pb, Bi, Zn, Cd. Later, they have been developed primarily to use in joining applications such as soldering or brazing industries due to its low melting point. Most aluminium-based casting alloys are developed based on eutectic systems for better castability to enable the manufacturing of engineering components for light-weighting design. Eutectic alloys offer desirable mechanical and magnetic properties for potential exploitation in structural and soft magnetic applications. Recently, eutectic alloys have been exploited as phase change material for latent heat thermal energy storage[8]. Finally, the emerging development of eutectic microstructure in equiatomic/near equiatomic multicomponent systems known as high entropy alloys (HEAs) has opened up the increasing research interest on eutectic alloys in high-order multicomponent systems, which provides an excellent opportunity to discover new materials with new properties.

2. Previous and current research of eutectic alloys

Eutectic solidification of binary alloys[910111213141516] involves the nucleation and growth of a two-phase mixture. The morphology of such regular two-phase eutectic microstructure (e.g. lamellar, rod-like, fibrous etc.) depends on materials characteristics such as faceted/non-faceted nature, entropy of fusion and proportion of each solid phase, as well as the solidification conditions[17,18]. Such two-phase eutectic microstructure is not limited to binary alloy systems but are also found in ternary (e.g.

Al-Si-Cu[19], Ag-Cu-Ge[20], Ti-Sn-Fe[2122], Co-Fe-Zr[12], Fe-Si-Ti[23], Fe-Ti-Zr[24]) and other quaternary[2526232427282930], quinary[273132333435363738] and senary[3940] multicomponent alloy systems. However, other multiphase eutectic microstructure beyond two-phase mixture have been observed in ternary (e.g. Al-Cu-Si[41,19,42], Al-Cu-Ag[42,43], Al-Ni-Mg[44], Nb-Al-Ni[45,46],Al-Cu-Ni[47], Fe-Mo-Si[48], Fe-B-Cu[49]) and quaternary (e.g. Al-Cu-Si-Mg[50]) eutectic alloys. There are hundreds or more eutectic/near eutectic alloys[51] found in metallic systems comprising of upto 6 constituents. Table 1 gives a selected list of these eutectic alloys from binary to senary systems. It is interesting to see that the total number of co-existed phases present in the eutectic microstructure is below four even for the senary alloys.

3. Search for eutectic composition.

Not all binary alloys can form eutectic alloys. This is because the valence electrons of the constituents are not always compatible with the formation of joint crystal lattice. However, these binary eutectic alloys are frequently formed at near simple composition ratio[52] of their constituents, such as 8/1, 5/1, 3/1, 2/1 and 3/2[53]. This was explained previously by the short-range atomic ordering of the eutectic liquid structure into specific arrangements of icosahedral clusters[53,54]. Recently, a new structural tool based on the cluster-plus-glue-atom model[55] was used to derive the composition formulas of binary eutectics. The eutectic compositions and temperatures of many binary and ternary alloys can be extracted from experimentally determined equilibrium phase diagrams listed in handbooks[56,57].

If all the eutectic phases formed are known beforehand, the eutectic composition and eutectic temperature, T_E, can be predicted using the following Schroeder-van Laar equation [58,59,60]:

$$Ln\, X_i = \frac{\Delta H^i_{fusion}}{R}\left(\frac{1}{T_E} - \frac{1}{T_i}\right)$$

where X_i is the molar fraction of the i^{th} phase, T_E is the eutectic temperature of the alloy and T_i is the melting temperature of the i^{th} phase. This approach has been applied to 16 binary (e.g. Al-Ga, Al-Ge-Al-Zn, Au-Ge, Pb-Sb etc.) and 6 ternary (e.g. Al-Ge-Sn, Cd-Pb-Sn etc.) eutectic alloys[61]. In general, the theoretic prediction agrees well with the general trends of eutectic temperature and compositions studied over a wide range of alloy systems. However, there are discrepancies between the predicted and the experimental data, which may be due to the assumption of ideal mixing in the Schroeder-van Laar equation. For quaternary alloys, the eutectic points can be determined by two-dimensional sections set construction[62] (tie-lines method) on the model of T-x-y-z and the intersection of the four surfaces of primary crystallization of the components based on data from binary and ternary alloy systems[59]. However, they rely on prior knowledge of all co-existed eutectic phases.

An alternative way to search the eutectic point, is to use the CALPHAD (CALculation of PHAse Diagrams) software (e.g. Thermocalc, Pandat, JMatPro, FactSage)[63], which is based on several geometric methods or mathematical formalisms to generate the phase diagrams. These programs use the properties of the individual

components, single points of experimental data of mixtures and high order thermodynamic database[64] by extrapolation from the lower order constituent binary and ternary systems. For quinary alloys, the phase diagrams can be computed by fixing four elements first and then adjusting the 5th element[65,66,67,68]. There is a still huge challenge to design/locate the eutectic compositions in high-order constituent alloy systems without prior knowledge of eutectic phases.

In our studies, the initial prediction of the eutectic composition of Al-Cu-Si-Mg quaternary alloy was determined using Thermocal software to achieve the lowest melting point for the solidification of a four-phase microstructure by adding Mg, together with the adjustment of Cu and Si contents of known ternary Al-Cu-Si ternary eutectic composition, as shown in Figure 1. The predicted eutectic composition of Al-Cu-Si-Mg was found to be Al-12at%Cu-7at%Si-3at%Mg. This is similar to the reported Al-14at%Cu-7at%Si-3at%Mg[50] eutectic composition.

4. From binary Al-Cu to quaternary Al-Cu-Si-Mg systems

Figure 2a shows DSC curves of suction cast $Al_{84}Cu_{16}$(binary), $Al_{81}Cu_{12}Si_7$(ternary) and $Al_{76}Cu_{14}Si_7Mg_3$(quaternary) eutectic alloys subjected to a 20K/min cooling cycle. They consisted of a single exothermic DSC peak, corresponding to eutectic solidification. The eutectic solidification peak occurs at 558°C in $Al_{84}Cu_{16}$ and decreases to 518°C in $Al_{76}Cu_{14}Si_7Mg_3$. The heats of fusion (i.e. area under the peak) of ternary and quaternary eutectic alloys are found to be 448J/g and 398J/g, respectively. This corresponds to the

decreasing eutectic temperature with increasing number of elements in the alloy system. The direct proportional relationship between melting temperature and heat of fusion has been reported in Al-Cu binary alloy[69]. Figure 2b shows XRD spectra of suction cast $Al_{84}Cu_{16}$, $Al_{81}Cu_{12}Si_7$ and $Al_{76}Cu_{14}Si_7Mg_3$ alloys. The number of eutectic phases increased from two (e.g. α-Al and θ-Al_2Cu) in binary to four (e.g. α-Al, θ-Al_2Cu, Si, Q($Al_4Cu_2Mg_8Si_7$)) in the quaternary alloys. α-Al and θ-Al_2Cu are two predominant eutectic phases present in all three alloys.

The as-cast microstructures of $Al_{84}Cu_{16}$, $Al_{81}Cu_{12}Si_7$ and $Al_{76}Cu_{14}Si_7Mg_3$ alloys consisted of a lamellar eutectic microstructure, as shown in Figures 3(a-d). The average interlamellar spacing reduced from 81.5±8nm in $Al_{84}Cu_{16}$ to 48.5±4nm in $Al_{76}Cu_{14}Si_7Mg_3$. However, both $Al_{81}Cu_{12}Si_7$ and $Al_{76}Cu_{14}Si_7Mg_3$ alloys comprised of cellular eutectic colonies separated by an intercellular region of nanometre-sized anomalous eutectic mixture free from any lamellar morphology. This suggests a decoupled growth of eutectic phases towards the end of the solidification process in ternary and quaternary eutectic alloys. The solute concentration varied from the centre of the cellular colony to the intercellular region. The intercellular region was found to be enriched in Si and deficient in Cu, as shown in Figure 2d as a result of solute redistribution during the solidification process. Similar Si enrichment in the intercellular region has also been reported in Al-Cu-Si ternary eutectic alloy[41]. The formation of cellular eutectic and anomalous eutectic regions in ternary and quaternary alloys is due to uncontrolled growth conditions associated with relatively high cooling rate (10^2-10^3K/s)[70] from suction casting process and the redistribution of additional atomic species such as Si, Mg. This can destabilise the solid/liquid interface (morphological instability) and

encourage non-cooperative eutectic growth to yield cellular and anomalous eutectic regions, respectively. The coarse regions at the cellular boundaries, is resulted from the volume fraction adjustment[45] between constitute phases due to multiple solute rejection from the solidifying eutectic. The refinement of the interlamellar spacing in quaternary eutectic alloy can be attributed to (1) slow atomic mobility and growth rate associated with low eutectic temperature and (2) increasing resistance to the formation of appropriate crystalline phases to maintain cooperative eutectic growth by the presence of many different atomic species in the melt.

The four-phase microstructure of cellular eutectic colonies in $Al_{76}Cu_{14}Si_7Mg_3$ alloy consisted of α-Al and θ-Al_2Cu lamellae, together with the fibrous Q-phase (e.g. 100-150nm width and 300-500nm length) growing along the θ-Al_2Cu phase and few 150-200nm Si particles trapped between Q and θ-Al_2Cu phases, as shown in Figures 4(a-c) and confirmed by SADPs (Figure 4d) corresponded to α-Al<1 0 0> , Si <0 0 1>,Q <1 1 $\overline{2}$ 9> and θ-Al_2Cu <1 1 0>, respectively. However, such four-phase microstructure changed to a mixture of equiaxed α-Al, θ-Al_2Cu and Si phases, together with platelets of Q phase, as shown in Figure 4c. The sizes of Si, θ-Al_2Cu and Q phases reduced to 40-90nm, 50-100nm and 100nm width by 100-250nm length, respectively.

The orientation relationship (OR) of eutectic θ-Al_2Cu, α-Al and Q phases in the cellular region exhibited the following orientation relationship as determined by T-EBSD technique (Figure 5):

$$\{211\}_{\theta-Al_2Cu}//\{111\}_{Al}\ //\{31\bar{4}0\}_Q\ and\ <120>_{\theta-Al_2Cu}//<110>_{Al}//<0001>_Q$$

The α-Al/θ-Al_2Cu eutectic phases in quaternary alloy retained a similar OR to that reported in binary Al-Cu system[9]. Hence in the (α-Al + θ-Al_2Cu+ Q-phase + Si) quaternary eutectic, Si faceted phase grows independently, while α-Al, θ-Al_2Cu and Q-phase grow cooperatively, maintaining the OR.

5. Multicomponent eutectic alloys beyond quaternary Al-Cu-Si-Mg system

Table 2 shows a list of multicomponent alloys prepared by suction casting and characterised in this study. Figure 6 shows DSC traces of these multicomponent alloys subjected to a 20K/min heating cycle. The 5-element multicomponent alloy consisted of a single endothermic peak, corresponding to the eutectic reaction. However, the DSC traces of 11-element and 13-element alloys consisted of multiple endothermic peaks overlapping each other. In all cases, solidification of primary phase from the melt has not been observed by DSC studies. However, the heat of fusion (i.e. area under the peak) of 5-element multicomponent alloy is 337J/g, which is higher than 257J/g in 11-element and 272J/g in 13-element alloys. This is contributed to the lower onset melting temperature of 11- and 13-element multicomponent alloys as compared to 5-element multicomponent alloy.

Figure 7a shows typical as-solidified microstructure of suction cast $Al_{77}Cu_{13}Si_6Mg_3Ni_1$ quinary alloy. It has a similar cellular eutectic microstructure (Figure 7b) with ultrafine eutectic mixture at the intercellular region (Figure 7c) as compared to that found in $Al_{76}Cu_{14}Si_7Mg_3$ quaternary alloy. From the SEM micrographs, a four-phase

eutectic microstructure was observed and it consisted of α-Al (light grey), θ-Al_2Cu (white), Q-phase (dark grey) as marked by a red circle in Figure 7b and Si (black). The Q-phase is formed on the θ-Al_2Cu lamella. According to calphad calculation from Thermocalc, this quinary alloy comprises of five phases at various proportion at room temperature. They are α-Al (51vol.%); θ-Al_2Cu (34vol.%); Q-phase (9.5vol.%); Si (4vol.%); and Al_3Ni (2vol.%). The absence of Al_3Ni phase in the microstructure of this alloy from the SEM studies can be attributed to a combination of low volume fraction and its similar contrast to θ-Al_2Cu phase. The coarsening of eutectic lamellae was also observed at the cell boundary. In addition, the proportions of these eutectic phases within the intercellular region are different from those within the cellular region due to solute redistribution and enrichment at the liquid/solid interface.

As the number of elements increased from 5 to 11, the as-solidified microstructure of $Al_{70.5}Cu_{18}Si_{0.9}$ $Mg_6Ca_{0.9}Fe_{0.2}Mn_{0.5}Ni_{0.8}Ti_{0.5}Zr_{0.1}Zn_{1.6}$ became complex, as shown in Figure 8 and deviated from those in binary, ternary, quaternary and quinary eutectic alloys. The microstructure of the 11-element multicomponent alloy consisted of small blocky intermetallic (white), α-Al (black) and coarse intermetallic compound (grey) phases, as shown in Figures 8a. At high magnification, lamellar eutectic mixture (black+grey) was found together with blocky phase (white), as shown in Figure 8b. The composition of blocky phase(white) was determined as Al-14at%Cu-3at%Mg-0.7at%Ni from EDX spectrum (Figure 8c). This is similar to T-phase (Al_6MgCu) intermetallic compound but with the incorporation of a minor amount Ni, giving Al_6(MgCuNi). However, the grey phase is an unknown compound but has a composition of Al-8 at%Cu-5at%Mg-2at%Ca-0.6%Ni-0.6at%Mn compound, as shown in EDX spectrum (Figure 8d).

The ratio of Al/Cu in this complex unknown compound is similar to $Cu_2Mn_3Al_{20}$ intermetallic compound but with a lower concentration of Mn, giving $Cu_2(MnMgCaNi)_3Al_{20}$. The lamellar eutectic region consisted of α-Al and Al-8at%Cu-5at%Mg-2at%Ca-0.6%Ni-0.6at%Mn multicomponent compound based on the contrast of the phase in the BSE-SEM micrograph, as shown in Figure 8b. The solidification of this 11-element multicomponent alloy may involve two stages: (a) formation of coarse phase mixture (e.g. α-Al, $Al_6(MgCuNi)$, $Al_{20}Cu_2(MgCaNiMn)_3$) at high temperature; and (b) a fine lamellar eutectic mixture (e.g. α-Al, $Al_{6(}MgCuNi)$) at low temperature. This is reflected by asymmetry of DSC melting peak of 11-element multicomponent alloy as shown in Figure 6.

In 13-element multicomponent alloy ($Al_{72}Cu_{17}Si_{0.9}Mg_{3.8}Ca_{0.7}Fe_{0.2}Mn_{0.7}Ni_{0.9}Ti_{0.4}Zr_{0.1}Ag_{1.6}Sn_{0.7}Zn_1$), the as-solidified microstructure consisted of three phases corresponding to grey, black and white regions, as shown in the BSE-SEM micrograph taken at a low magnification (Figure 9a). However, at high magnification (Figure 9b), it revealed a complex microstructure comprised of three interconnected phases corresponding to black, light and dark grey regions, together pockets of fine two-phase lamellar morphology, corresponding to white and dark regions. However, X-ray maps obtained from the FIB-SEM specimen showed a very complex microstructure, consisting of seven phases including Al-, Cu-, Zr-, Ti-, Si, Ag-Zn, Mg-Ca-Sn, Ni-Fe-Mn, as shown in Figure 10. The Al-rich and Cu-containing phases corresponded to α-Al and Al_2Cu phases with compositions of Al-5.6at%Cu-5.4at%Mg-1.2at%Si-0.3at%Ca-0.4at%Ni-0.7at%Zr-0.5at%Mn-0.2at%Fe-0.2at%Ti-0.3at%Ag-0.3at%Sn-0.2at%Zn(Figure 11a) and Al-33at%Cu-2.3at%Mg-0.3at%Si-0.7at%Ca-1.8at%Ni-1at%Mn-0.6at%Fe-0.7at%-0.9at%Ag-

0.6at%Sn-0.9at%Zn (Figure 11b), respectively. There are four Ag-Zn intermetallic compounds[71] and one ternary Mg-Ca-Zn intermetallic compound[72]. Ternary Fe-Mn-Ni phase can exist as solid solution if the composition is located near the Fe corner of the ternary alloy system[73], while Zr- and Ti- containing phases are unknown and yet to be identified. The formation of these phases involves three stages as illustrated by the three overlapping DSC melting peaks in Figure 6. The solidification behaviour of such alloy is very complex and further studies are being carried out to understand their microstructural evolution.

6. Hardness of binary eutectic to multicomponent alloys

The combination of refined microstructure and presence of Q-phase has led to the moderate increase in average hardness from 267HV in $Al_{84}Cu_{16}$ to 292HV in $Al_{77}Cu_{13}Si_6Mg_3Ni_1$, as shown in Figure 12. However, 11- and 13-elements multicomponent alloys exhibited average hardness values of 367HV and 380HV, respectively. Such significant increase in hardness is contributed by a complex microstructure of multiple phases including solid solutions and intermetallic compounds.

7. Conclusions

This review article has shown our strong understanding and knowledge of eutectic alloys in the low order constituent binary and ternary systems. When the alloy systems

become more complex and are based on a large number of constituents, our knowledge of eutectic solidification is limited and it is restricted mainly to two-phase eutectic microstructure. This is partly due to the difficulty of finding eutectic compositions in high order constituent alloy systems without any prior knowledge of co-existed eutectic phases. Our recent attempt to search for eutectic compositions in alloy systems beyond five constituents have led to the following conclusions:

- The melting temperature and latent heat of fusion decreased with increasing number of components in the alloy system.
- Ternary, quaternary and quinary eutectic alloys exhibited a similar microstructure of cellular colonies of lamellar morphology with ultrafine intercellular eutectic mixture.
- The as-solidified microstructure of 11- and 13-element multicomponent alloys comprised of multiple (e.g. 3-7) phases including solid solutions and intermetallic compounds.
- The average hardness increased with increasing number of components in the alloy systems.

This work has identified the knowledge gap of eutectic point(s) within the large composition space of high order multicomponent alloys. The newly studied multicomponent alloys offer superior hardness due to their complex multiphase microstructure. Finally, this opens up a novel approach to designing high strength aluminium based multicomponent alloys.

8. Acknowledgement

The authors would like to thank EPSRC for the financial support on Future Liquid Metal Engineering (LiME) Hub at BCAST, where this work was carried out. We would also like to thank Professor Z. Fan for the provision of processing and characterisation facilities at BCAST and the fruitful discussion on multicomponent eutectic alloys. Qing Cai is very grateful to Brunel University London for the financial support on his PhD studies. Finally, we would like to thank the Experimental Technique Centre(ETC) at Brunel University London for the provision of the electron microscopy characterisation facilities.

References

1. Guthrie, F. To cite this article: Frederick Guthrie (1884) LII. Onï¿¿eutexia , The London, Edinburgh, and Dublin Philosophical Magazine and. *J. Sci.* **17**, 462–482 (2010).
2. Fisher, D. J. & Kurz, W. A theory of branching limited growth of irregular eutectics. *Acta Metall.* **28**, 777–794 (1980).
3. Huang, W. & Wang, L. Solidification researches using transparent model materials - A review. *Sci. China Technol. Sci.* **55**, 377–386 (2012).
4. Orera, V. M., Peña, J. I., Oliete, P. B., Merino, R. I. & Larrea, A. Growth of eutectic ceramic structures by directional solidification methods. *J. Cryst. Growth* **360**, 99–104 (2012).
5. Jackson, K. A. & Hunt, J. D. Lamellar and Rod Eutectic Growth. *Trans. Metall. Soc. AIME* **236**, 1966–1129 (1966).
6. Hellawell, A. The growth and structure of eutectics with silicon and germanium. *Prog. Mater. Sci.* **15**, 3–78 (1970).
7. Shamsuzzoha, M. & Hogan, L. M. Crystal morphology of unmodified aluminium-silicon eutectic microstructures. *J. Cryst. Growth* **76**, 429–439 (1986).
8. Risueño, E. *et al.* Mg-Zn-Al Eutectic Alloys as Phase Change Material for Latent Heat Thermal Energy Storage. in *Energy Procedia* **69**, 1006–1013 (Elsevier Ltd, 2015).

9. Cantor, B. & Chadwick, G. A. The growth crystallography of unidirectionally solidified Al-Al3Ni and Al-Al2Cu eutectics. *J. Cryst. Growth* **23**, 12–20 (1974).

10. Cantor, B. & Chadwick, G. A. The tensile deformation of unidirectionally solidified Al-Al3Ni and Al-Al2Cu eutectics. *J. Mater. Sci.* **10**, 578–588 (1975).

11. Hecht, U., Witusiewicz, V., Drevermann, A. & Rex, S. Formation of Eutectic Cells in Ternary Al-Cu-Ag Alloys. *Solidif. Cryst.* 259–270 (2005). doi:10.1002/3527603506.ch28

12. Manjura Hoque, S., Makineni, S. K., Pal, A., Ayyub, P. & Chattopadhyay, K. Structural and magnetic properties of ultra-small scale eutectic CoFeZr alloys. *J. Alloys Compd.* **620**, 442–450 (2015).

13. Yang, C., Zhang, J., Huang, H., Song, Q. & Liu, F. Stability of metastable phase and soft magnetic properties of bulk Fe-B nano-eutectic alloy prepared by undercooling solidification combined with CU-mold chilling. *Phys. B Condens. Matter* **476**, 132–136 (2015).

14. Park, J. M. *et al.* Nanostructure-dendrite composites in the Fe-Zr binary alloy system exhibiting high strength and plasticity. *Scr. Mater.* **57**, 1153–1156 (2007).

15. Gogebakan, M., Kursun, C., Gunduz, K. O., Tarakci, M. & Gencer, Y. Microstructural and mechanical properties of binary Ni-Si eutectic alloys. *J. Alloys Compd.* **643**, S219–S225 (2015).

16. Louzguine, D. V., Kato, H., Louzguina, L. V. & Inoue, A. High-strength binary Ti-Fe bulk alloys with enhanced ductility. *J. Mater. Res.* **19**, 3600–3606 (2004).

17. Campbell, F. C. Ch 5. Eutectic Alloy Systems. 87–116 (2012).

18. Chanda, B., Potnis, G., Jana, P. P. & Das, J. A review on nano-/ultrafine advanced eutectic alloys. *J. Alloys Compd.* **827**, 154226 (2020).

19. Ruan, Y. & Wei, B. B. Rapid solidification of undercooled Al-Cu-Si eutectic alloys. *Chinese Sci. Bull.* **54**, 53–58 (2009).

20. Zhai, W., Lu, X. & Wei, B. Microstructural evolution of ternary Ag33Cu42Ge25 eutectic alloy inside ultrasonic field. *Prog. Nat. Sci. Mater. Int.* **24**, 642–648 (2014).

21. Park, E. M. *et al.* Solid-state phase transformation-induced heterogeneous duplex structure in Ti-Sn-Fe alloys. *J. Alloys Compd.* **515**, 86–89 (2012).

22. Das, J., Kim, K. B., Baier, F., Löser, W. & Eckert, J. High-strength Ti-base ultrafine eutectic with enhanced ductility. *Appl. Phys. Lett.* **87**, 1–3 (2005).

23. Park, J. M., Kim, D. H., Kim, K. B. & Eckert, J. Improving the plasticity of a high strength Fe-Si-Ti ultrafine composite by introduction of an immiscible element. *Appl. Phys. Lett.* **97**, 2008–2011 (2010).

24. Park, J. M., Kima, D. H., Kim, K. B., Mattern, N. & Eckert, J. Evolution of

constitution, structure, and mechanical properties in Fe-Ti-Zr-B heterogeneous multiphase composites. *J. Mater. Res.* **26**, 365–371 (2011).

25. Baker, I., Wu, M. & Wang, Z. Eutectic/eutectoid multi-principle component alloys: A review. *Materials Characterization* **147**, 545–557 (2019).

26. He, F. *et al.* Grouping strategy in eutectic multi-principal-component alloys. *Mater. Chem. Phys.* **221**, 138–143 (2019).

27. Jin, X., Zhou, Y., Zhang, L., Du, X. & Li, B. A new pseudo binary strategy to design eutectic high entropy alloys using mixing enthalpy and valence electron concentration. *Mater. Des.* **143**, 49–55 (2018).

28. Lu, Y. *et al.* Directly cast bulk eutectic and near-eutectic high entropy alloys with balanced strength and ductility in a wide temperature range. *Acta Mater.* **124**, 143–150 (2017).

29. Rogal, L., Morgiel, J., Światek, Z. & Czerwiński, F. Microstructure and mechanical properties of the new Nb25Sc25Ti25Zr25 eutectic high entropy alloy. *Mater. Sci. Eng. A* **651**, 590–597 (2016).

30. Jin, X. *et al.* A new CrFeNi2Al eutectic high entropy alloy system with excellent mechanical properties. *J. Alloys Compd.* **770**, 655–661 (2019).

31. Dong, Y., Lu, Y., Kong, J., Zhang, J. & Li, T. Microstructure and mechanical properties of multi-component AlCrFeNiMo x high-entropy alloys. *J. Alloys Compd.* **573**, 96–101 (2013).

32. Guo, Y. *et al.* A superfine eutectic microstructure and the mechanical properties of CoCrFeNiMox high-entropy alloys. *J. Mater. Res.* **33**, 3258–3265 (2018).

33. Jiang, L. *et al.* Effect of Mo and Ni elements on microstructure evolution and mechanical properties of the CoFeNixVMoy high entropy alloys. *J. Alloys Compd.* **649**, 585–590 (2015).

34. Jiang, L. *et al.* Effects of Nb addition on structural evolution and properties of the CoFeNi2V0.5 high-entropy alloy. *Appl. Phys. A Mater. Sci. Process.* **119**, 291–297 (2015).

35. Vrtnik, S. *et al.* Magnetism of CoCrFeNiZrx eutectic high-entropy alloys. *Intermetallics* **93**, 122–133 (2018).

36. Jiang, H. *et al.* Microstructures and mechanical properties of Co2MoxNi2VWx eutectic high entropy alloys. *Mater. Des.* **109**, 539–546 (2016).

37. Lu, Y. *et al.* A new strategy to design eutectic high-entropy alloys using mixing enthalpy. *Intermetallics* **91**, 124–128 (2017).

38. Baker, I., Meng, F., Wu, M. & Brandenberg, A. Recrystallization of a novel two-phase FeNiMnAlCr high entropy alloy. *J. Alloys Compd.* **656**, 458–464 (2016).

39. Tan, Y., Li, J., Wang, J. & Kou, H. Seaweed eutectic-dendritic solidification

pattern in a CoCrFeNiMnPd eutectic high-entropy alloy. *Intermetallics* **85**, 74–79 (2017).

40. Ma, S. G. & Zhang, Y. Effect of Nb addition on the microstructure and properties of AlCoCrFeNi high-entropy alloy. *Mater. Sci. Eng. A* **532**, 480–486 (2012).

41. Park, J. M. *et al.* High-strength bulk Al-based bimodal ultrafine eutectic composite with enhanced plasticity. *J. Mater. Res.* **24**, 2605–2609 (2009).

42. Morando, C., Garbellini, O., Fornaro, O. & Palacio, H. Morphology and phase formation during the solidification of alcusi ternary eutectic system. *65th ABM Int. Congr. 18th IFHTSE Congr. 1st TMS/ABM Int. Mater. Congr. 2010* **6**, 4610–4617 (2010).

43. Mccartney, D. G., Jordan, R. M. & Hunt, J. D. *The Structures Expected in a Simple Ternary Eutectic System: Part I1. The Al-Ag-Cu Ternary System*.

44. Semenova, E. L. Aluminium – Magnesium – Nickel. 150–156 (1991).

45. Rios, C. T., Milenkovic, S., Gama, S. & Caram, R. Influence of the growth rate on the microstructure of a Nb-Al-Ni ternary eutectic. *J. Cryst. Growth* **237**–**239**, 90–94 (2002).

46. Contieri, R. J., Rios, C. T., Zanotello, M. & Caram, R. Growth and three-dimensional analysis of a Nb-Al-Ni ternary eutectic. *Mater. Charact.* **59**, 693–699 (2008).

47. Tiwary, C. S., Kashyap, S. & Chattopadhyay, K. Development of alloys with high strength at elevated temperatures by tuning the bimodal microstructure in the Al-Cu-Ni eutectic system. *Scr. Mater.* **93**, 20–23 (2014).

48. Lu, X. Y., Wang, W. L. & Zhai, W. Ternary eutectic and peritectic solidification of undercooled liquid Fe-Mo-Si alloys. *Mater. Charact.* **110**, 252–257 (2015).

49. Huang, H., Yang, C., Song, Q., Ye, K. & Liu, F. Nano-eutectic structure formation and soft magnetic properties of bulk ternary Fe-B-M (M = Si, Cu) alloys. *J. Appl. Phys.* **120**, 0–7 (2016).

50. Kaygısız, Y. & Maraşlı, N. Directional solidification of Al–Cu–Si–Mg quaternary eutectic alloy. *J. Alloys Compd.* **721**, 764–771 (2017).

51. Chanda, B., Potnis, G., Jana, P. P. & Das, J. A review on nano-/ultrafine advanced eutectic alloys. *J. Alloys Compd.* **827**, (2020).

52. Stockdale, D. Numerical relationships in binary metallic systems. *Proc. R. Soc. London. Ser. A - Math. Phys. Sci.* **152**, 81–104 (1935).

53. Hume-Rothery, W. & Anderson, E. Eutectic compositions and liquid immiscibility in certain binary alloys. *Philos. Mag.* **5**, 383 (1960).

54. Frank, F. C. Supercooling of Liquids. *Proc. Roy. Soc. London, Ser. A, Math. Phys. Sci.* **215**, 43–46 (1952).

55. Ma, Y. P. *et al.* Composition formulas of binary eutectics. *Sci. Rep.* **5**, 1–16 (2015).

56. *Binary Alloy Phase Diagrams, 2nd edition*. (ASM International, 1990).

57. *Handbook of Ternary Alloy Phase Diagrams*. **3**, (ASM International, 1995).

58. Ivashchenko, A. V., Titov, V. V. & Kovshev, E. I. Liquid Crystalline Compounds - 3. on Applicability of Schroeder - Van Laar Equations To Liquid Crystals Mixtures. *Mol Cryst Liq Cryst* **33**, 195–200 (1976).

59. Mamedov, A. N. & Mekhdiev, I. G. Prediction of the quaternary eutectic. *Thermochim. Acta* **269**–**270**, 73–78 (1995).

60. A. V. IVASHCHENKO, V. V. T. and E. I. K. Molecular Crystals and Liquid Crystals Liquid Crystalline Compounds: III On Applicability of Schröder-Van Laar Equations to Liquid Crystals Mixtures. *Molelcular Cryst. Liq. Cryst.* **33**, 195–200 (1976).

61. Ding, Z. Y., He, Q. F. & Yang, Y. Exploring the design of eutectic or near-eutectic multicomponent alloys: From binary to high entropy alloys. *Sci. China Technol. Sci.* **61**, 159–167 (2018).

62. Lutsyk, V. I., Zelenaya, A. E., Savinov -, V. V, Sumkina, O. G. & Savinov, V. V. Precision of the eutectic points determination by the isopleths. in *IOP Conference Series: Materials Science and Engineering 18* 162021 (2011). doi:10.1088/1757-899X/18/16/162021

63. Raud, R., Jacob, R., Bruno, F., Will, G. & Steinberg, T. A. A critical review of eutectic salt property prediction for latent heat energy storage systems. *Renewable and Sustainable Energy Reviews* **70**, 936–944 (2017).

64. Farkas D, B. C. New eutectic alloys and their heats of transformation. Metallurgical and Materials Transactions A 1985. *Metall. Trans. a* **16A**, 323 (1985).

65. Zhang, C., Zhang, F., Chen, S. & Cao, W. Computational Thermodynamics Aided High-Entropy Alloy Design. *JOM* **64**, 839 (2012).

66. Hsu, C.-Y. *et al.* Phase Diagrams of High-Entropy Alloy System Al-Co-Cr-Fe-Mo-Ni. *JoM* **65**, 1829 (2013).

67. Zhang, F. *et al.* An understanding of high entropy alloys from phase diagram calculations. *Calphad Comput. Coupling Phase Diagrams Thermochem.* **45**, 1–10 (2014).

68. Zhang, C. *et al.* Understanding phase stability of Al-Co-Cr-Fe-Ni high entropy alloys. *Mater. Des.* **109**, 425–433 (2016).

69. Zhao, J., Yuan, Y. & Cui, • Fu. Relationship between the Cu content and thermal properties of Al-Cu alloys for latent heat energy storage. (2017). doi:10.1007/s10973-017-6153-3

70. Srivastava, R. M., Eckert, J., Löser, W., Dhindaw, B. K. & Schultz, L. *Cooling Rate Evaluation for Bulk Amorphous Alloys from Eutectic Microstructures in Casting Processes*. *Materials Transactions* **43**, (2002).

71. Palenzona, A., Manfrinetti, P. & Fornasini, M. L. Phase diagram of the Ca-Sn system. *J. Alloys Compd.* **312**, 165–171 (2000).

72. Hort, N., Huang, Y. D., Leil, T. A., Rao, K. P. & Kainer, K. U. Properties and processing of magnesium-tin-calcium alloys. *Kov. Mater.* **49**, 163–177 (2011).

73. Pustov, L. Y. *et al.* Structure and phase transformations in Fe-Ni-Mn alloys nanostructured by mechanical alloying. *J. Alloys Compd.* **483**, 200–203 (2009).

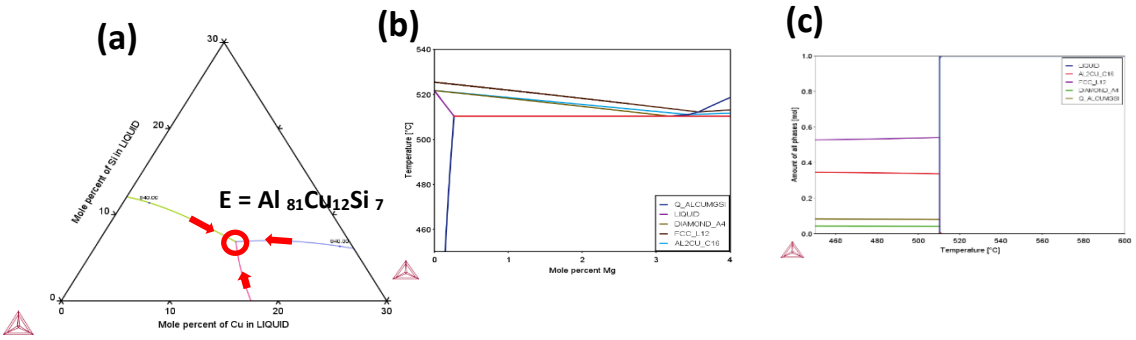

Figure 1. Thermocalc prediction of Al-Cu-Si equilibrium phase diagram (a), vertical section from ternary $Al_{81}Cu_{12}Si_7$ with increasing Mg content (b) and fraction of solid phases as a function of temperature at predicted quaternary $Al_{77}Cu_{12}Si_7Mg_3$ eutectic composition(c).

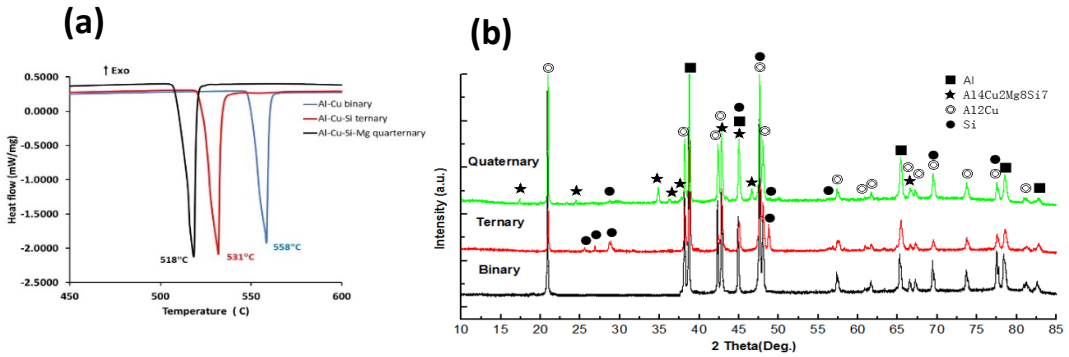

Figure 2 DSC traces (a) and XRD spectra (b) of suction cast $Al_{84}Cu_{16}$(binary), $Al_{81}Cu_{12}Si_7$(ternary) and $Al_{76}Cu_{14}Si_7Mg_3$(quaternary) alloys.

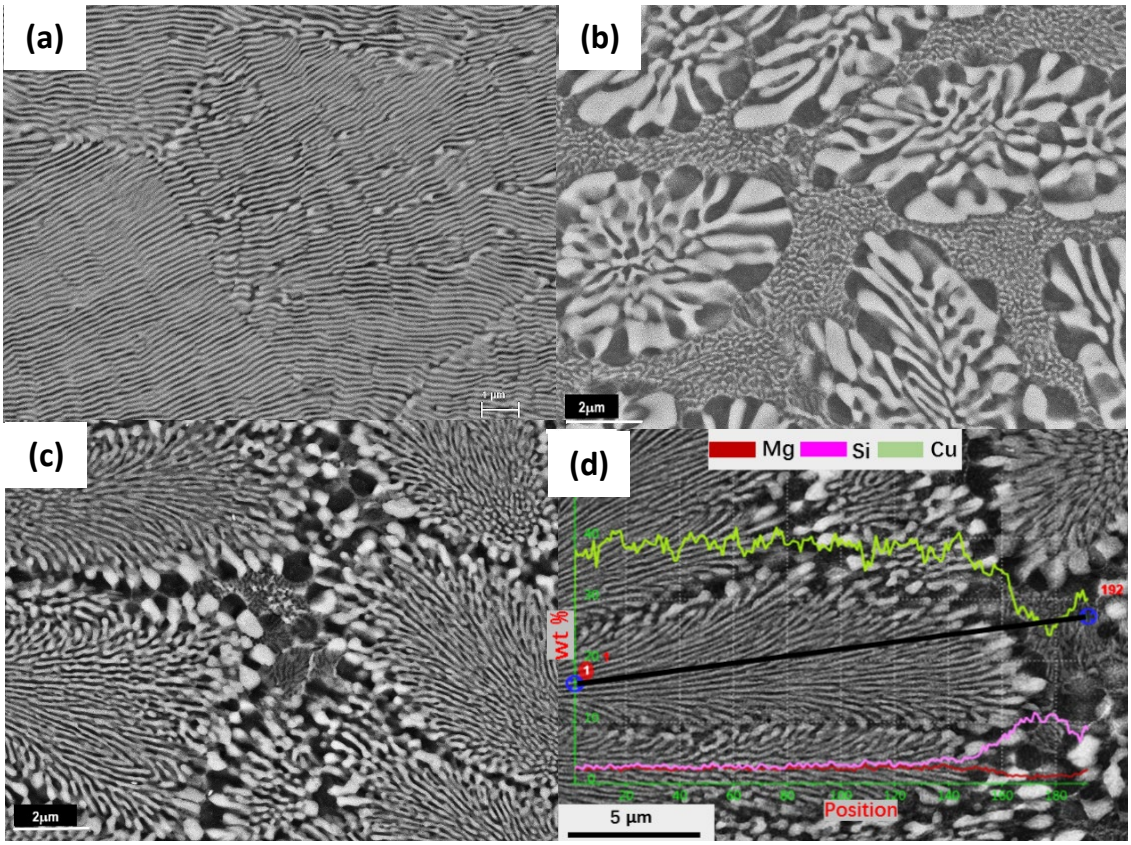

Figure 3 SEM micrographs of suction cast $Al_{84}Cu_{16}$ (a), $Al_{81}Cu_{12}Si_7$ (b) and $Al_{76}Cu_{14}Si_7Mg_3$ (c-d) alloys

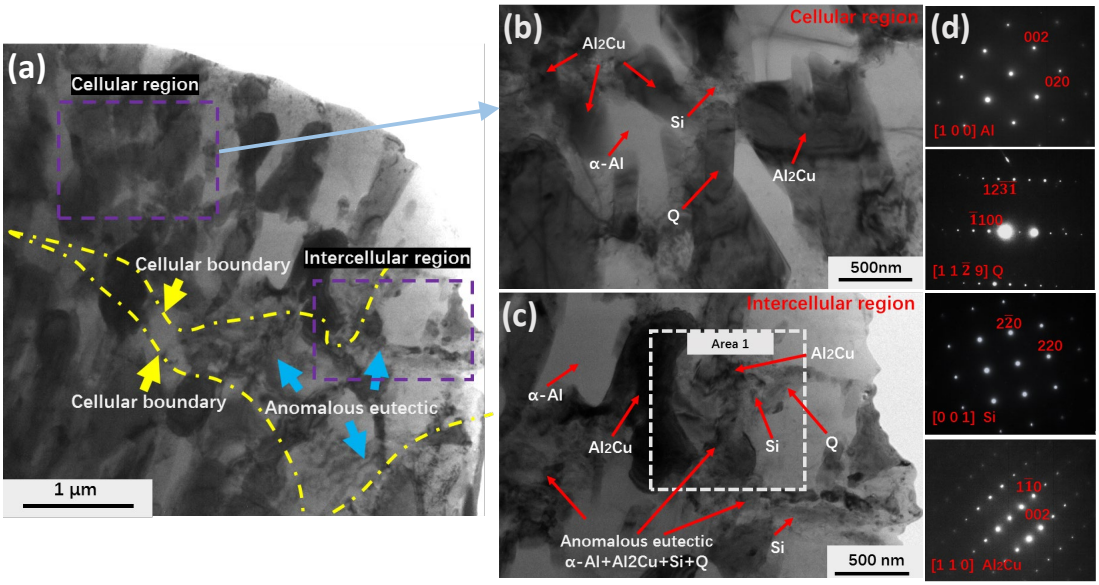

Figure 4 TEM bright-field micrographs of $Al_{76}Cu_{14}Si_7Mg_3$: (a) cellular and intercellular regions; (b) cellular eutectic region with corresponding (c) intercellular region and (d) SADPs of eutectic phases.

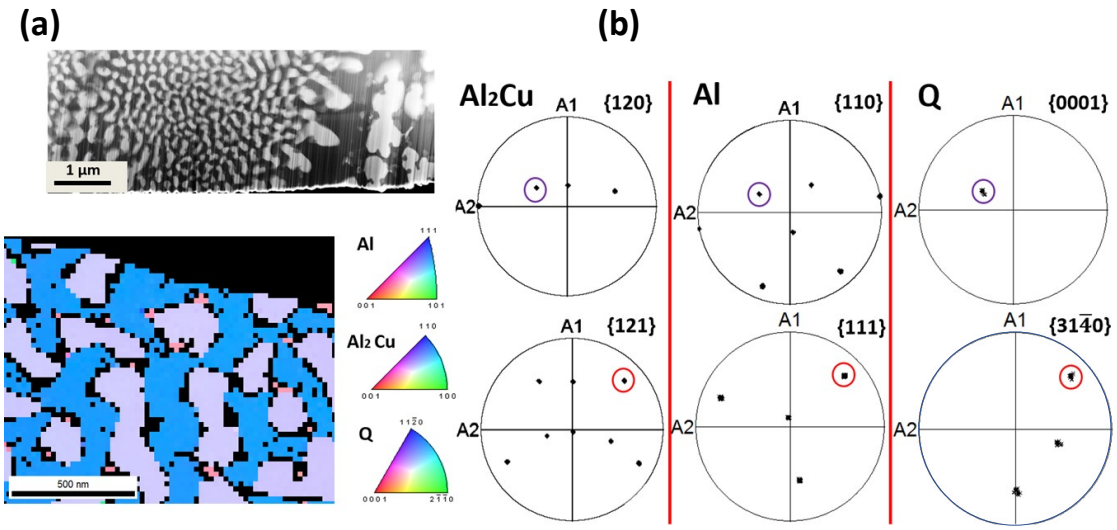

Figure 5 T-EBSD and inverse pole figure map of suction cast $Al_{76}Cu_{14}Si_7Mg_3$ (a) and identification of the orientation relationship between eutectic α-Al, θ-Al_2Cu and Q phases present in the centre of cellular region (b).

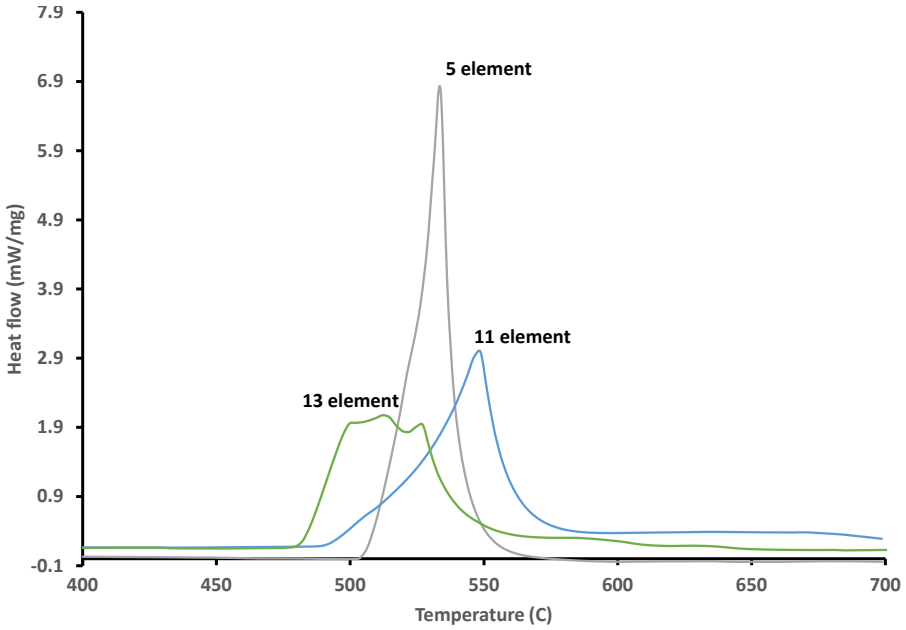

Figure 6 DSC traces of 5-, 11- and 13-element multicomponent alloys obtained from heating at a rate of 20K/min.

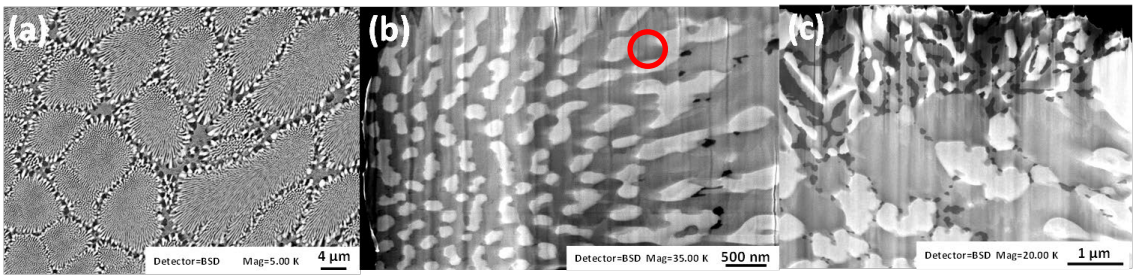

Figure 7 SEM micrograph of cellular eutectic microstructure in suction cast quinary $Al_{77}Cu_{13}Si_6Mg_3Ni_1$ alloy (a), together with FIB-SEM micrographs of the cell (b) and cellular boundary (c) regions taken using the in-lens detector.

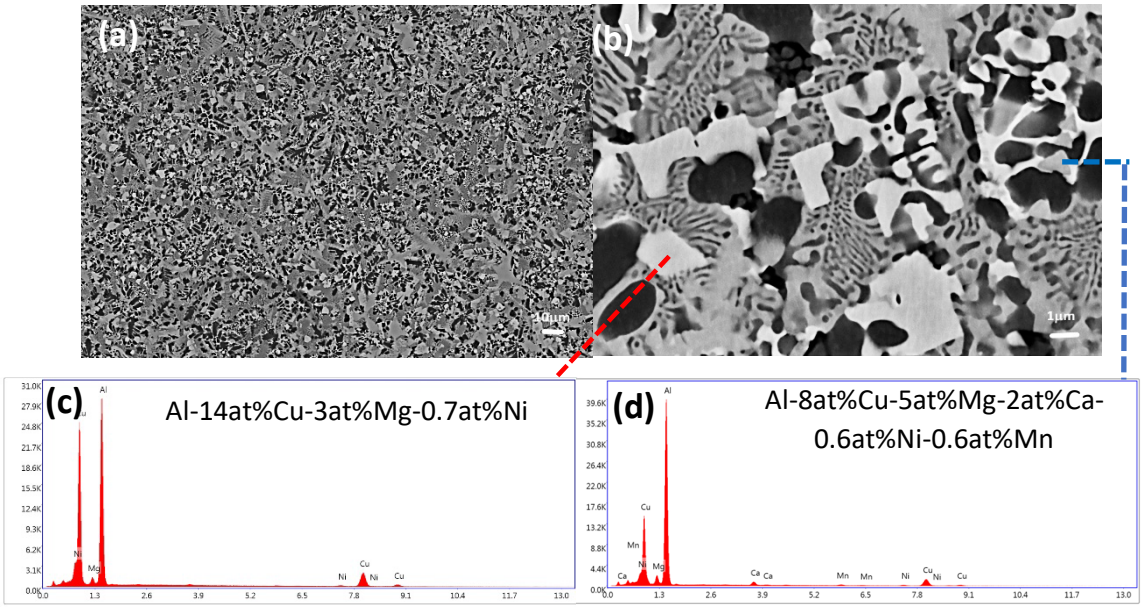

Figure 8 BSE-SEM micrographs of 11-element multicomponent alloy taken at low magnification (a) and high magnification (b) together with EDX spectra of white (c) and grey (d) regions.

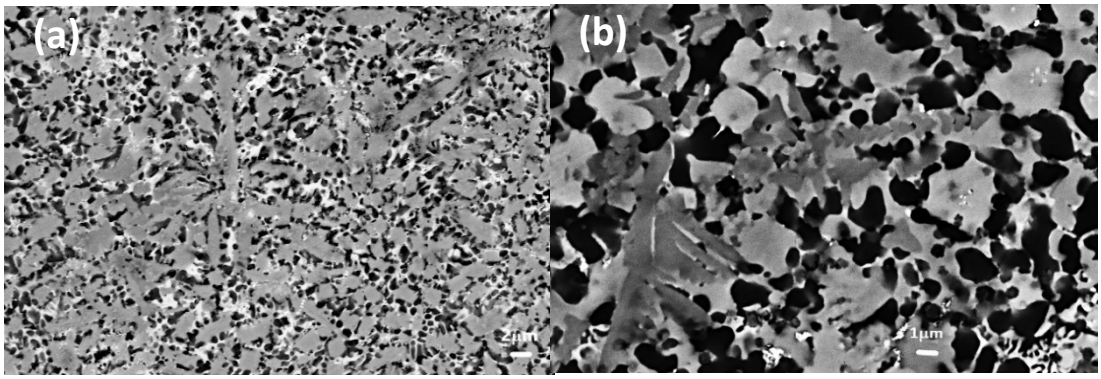

Figure 9 BSE-SEM micrographs of 13-element multicomponent alloy taken as low magnification (a) and high magnification (b).

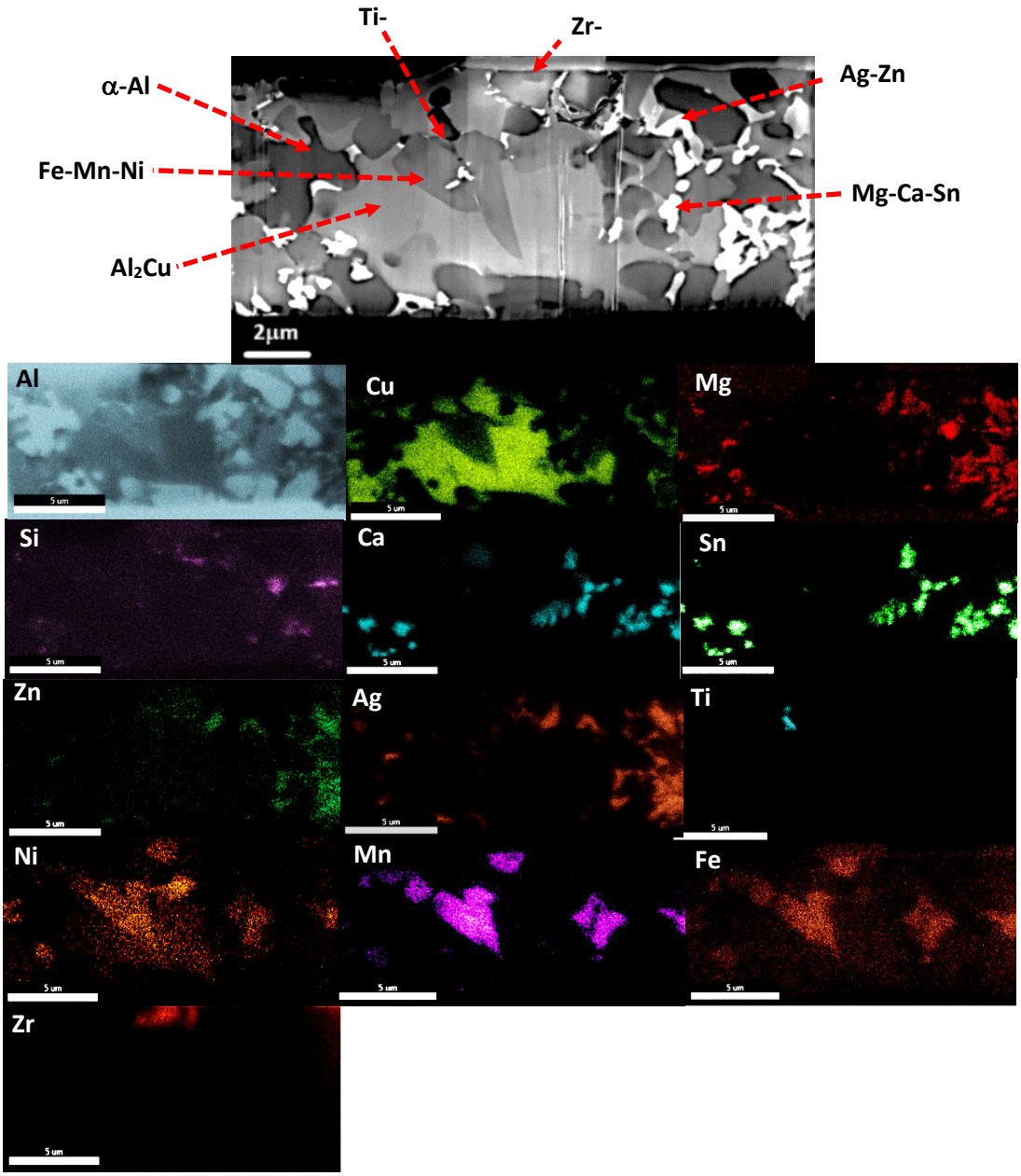

Figure 10 FIB-SEM micrograph of Al $_{72}Cu_{17}Si_{0.9}Mg_{3.8}Ca_{0.7}Fe_{0.2}Mn_{0.7}Ni_{0.9}Ti_{0.4}Zr_{0.1}Ag_{1.6}Sn_{0.7}Zn_1$ alloy, together with X-ray maps showing the corresponding element within each phase.

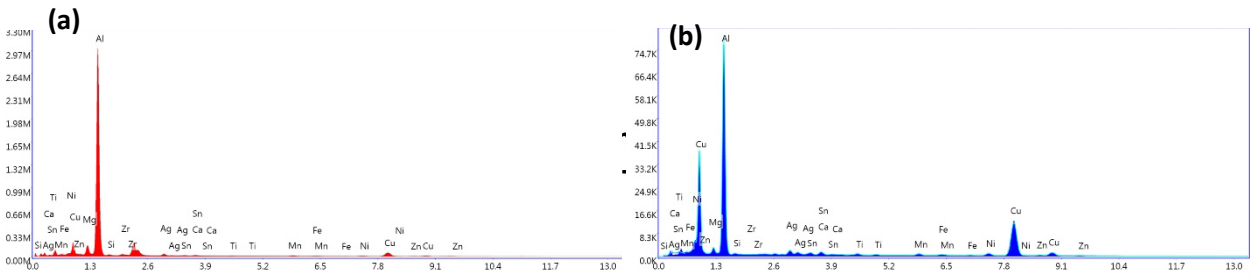

Figure 11 EDX spectra of Al-rich (a) and Cu-containing phases in Al $_{72}Cu_{17}Si_{0.9}Mg_{3.8}Ca_{0.7}$ $Fe_{0.2}Mn_{0.7}Ni_{0.9}Ti_{0.4}Zr_{0.1}Ag_{1.6}Sn_{0.7}Zn_1$ alloy

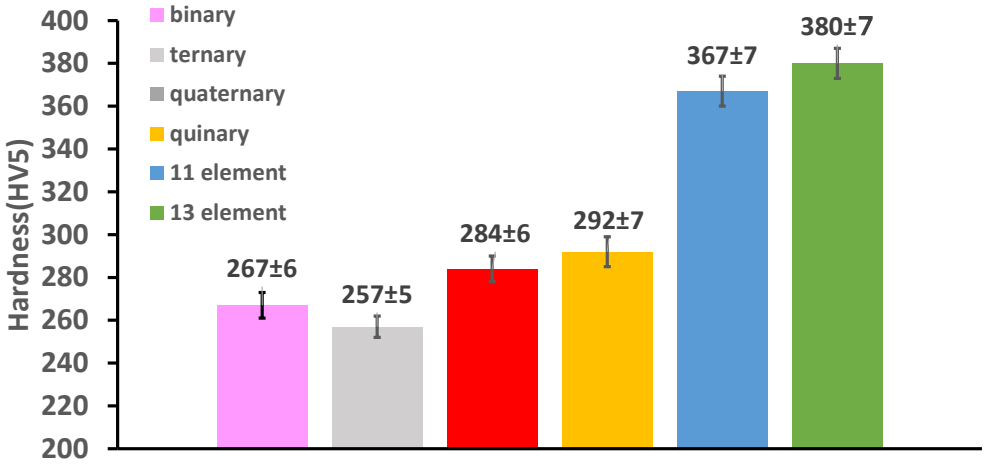

Figure 12 A plot of average Vickers Hardness of suction cast alloys from binary to 13-element multicomponent systems.

Table 1 A selected range of studied eutectic alloys from low to high order constituent systems

Alloy	Phases	References
Binary		
$Al_{84}Cu_{16}$	α-Al+ Al_2Cu	[9] [10]
$Al_{61}Ag_{39}$	α-Al +	[11]
$Al_{96.9}Ni_{3.1}$	α-Al + Al3Ni	[9]
$Co_{90.5}Zr_{9.5}$	HCP Co + $Co_{11}Zr_2$	[12]
$Fe_{83}B_{17}$ (annealed)	α-Fe + Fe_2B	[13]
$Fe_{90.2}Zr_{9.8}$	BCC Fe + $Fe_{23}Zr_6$	[12]
$Fe_{90}Nb_{10}$	α-Fe+Fe_2Nb	[14]
$Ni_{80}Si_{20}$	δ-Ni_2Si + γ-$Ni_{31}Si_{12}$	[15]
$Ni_{55}Si_{45}$	γ-$Ni_{31}Si_{12}$ + NiSi	[15]
$Ni_{70}Si_{30}$	δ-Ni_2Si + γ-$Ni_{31}Si_{12}$	[15]
$Ni_{45}Si_{55}$	α-$NiSi_2$ + NiSi	[15]
$Ti_{70.5}Fe_{29.5}$	β-Ti + TiFe	[16]
Ternary		
$Al_{76.07}Cu_{13.6}$ $Ag_{10.27}$	α-Al +θ-Al_2Cu + δ-$AlAg_2$	[43]
$Al_{64.6}Mg_{34.6}Ni_{0.8}$	α-Al + $NiAl_3$ + Mg_2Al_3	[44]
$Al_{81}Cu_{13}Si_6$	α-Al+ θ-Al_2Cu+Si	[41,19,42]

$Co_{49.2}Fe_{49.2}Zr_{9.6}$	BCC Co(Fe) + $Co(Fe_{23}Zr_6)$	[12]
$Fe_{83}B_{16}Si_1$	α-Fe(Si) +Fe_3B +Fe_2B	[49]
$Fe_{83}B_{16}Cu_1$	α-Fe(Cu) +Fe_3B +Fe_2B	[49]
$Fe_{75}Si_{15}Ti_{10}$	α-Fe(Si) + $(Fe,Si)_2Ti$	[23]
$Fe_{87}Ti_7Zr_6$	α-Fe +Fe_2Ti	[24]
$Ti_{67.79}Fe_{28.36}Sn_{3.85}$	β-Ti + FeTi	[2122]
Quaternary		
$Al_{77}Cu_{12}Si_7Mg_3$	α-Al + θ-Al_2Cu + Si + $Q(Al_4Cu_2Mg_8Si_7)$	[50]
$CoCrFeNi_{2.1}$	FCC + B2	[28]
$Fe_{71}Si1_5Ti_{10}Cu_4$	α-Fe(Si) + $(Fe,Si)_2Ti$	[23]
$Fe_{81}Ti_7Zr_6B_6$	α-Fe +Fe_2Ti	[24]
$Nb_{25}Sc_{25}Ti_{25}Zr_{25}$	HCP + BCC	[29]
$CrFeNi_2Al_{0.8}$	FCC + B2/BCC	[30]
Quinary		
$AlCrFeNiMo_{0.2}$	FeCr type solid solution + AlNi intermetallic compound	[31]
$AlCoCrFeNi_3$	B2 + FCC ($L1_2$)	[27]
$AlCo_2CrFeNi_2$	B2+FCC ($L1_2$)	[27]
$Fe_{28.2}Ni_{18.8}Mn_{32.9}Al_{14.1}Cr_6$	FeMn + NiAl	[38]
$CoCrFeNiMo_{0.8}$	FCC + $Cr_9Mo_{21}Ni_{20}$	[32]
$CoFeNi_{1.4}VMo$	FCC + Co_2Mo_3	[33]

$CoFeNi_2V_{0.5}Nb_{0.75}$	FCC +Fe_2Nb type Laves	[34]
$CoCrFeNiZr_{0.45}$	γ-Fe FCC + $ZrCo_2$ type Laves	[35]
$Co_2Mo_{0.6}Ni_2VW_{0.8}$	FCC + Co_7Mo_6-type μ phase	[36]
$Hf_{0.55}CoCrFeNi_2$	FCC + Ni_7Hf_2	[37]
$Ta_{0.65}CoCrFeNi_2$	FCC + $(Co,Ni)_2Ta$	[37]
$Zr_{0.6}CoCrFeNi_2$	FCC + Ni_7Zr_2	[37]
Senary		
CoCrFeNiMnPd	CoCrFeNi + Mn_7Pd_9	[39]
$AlCoCrFeNiNb_{0.6}$	(CoCr)Nb + BCC	[40]

Table 2 A list of multicomponent alloys studied

Number of components	**Alloy composition (at.%)**
5	$Al_{77}Cu_{13}Si_6Mg_3Ni_1$
11	$Al_{70.5}Cu_{18}Si_{0.9}Mg_6Ca_{0.9}Fe_{0.2}Mn_{0.5}Ni_{0.8}Ti_{0.5}Zr_{0.1}Zn_{1.6}$
13	$Al_{72}Cu_{17}Si_{0.9}Mg_{3.8}Ca_{0.7}Fe_{0.2}Mn_{0.7}Ni_{0.9}Ti_{0.4}Zr_{0.1}Ag_{1.6}Sn_{0.7}Zn_1$

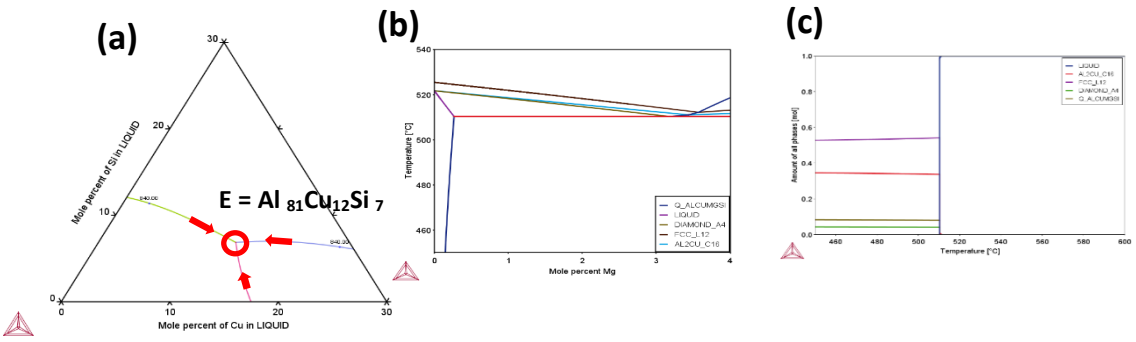

Figure 1. Thermocalc prediction of Al-Cu-Si equilibrium phase diagram (a), vertical section from ternary $Al_{81}Cu_{12}Si_7$ with increasing Mg content (b) and fraction of solid phases as a function of temperature at predicted quaternary $Al_{77}Cu_{12}Si_7Mg_3$ eutectic composition(c).

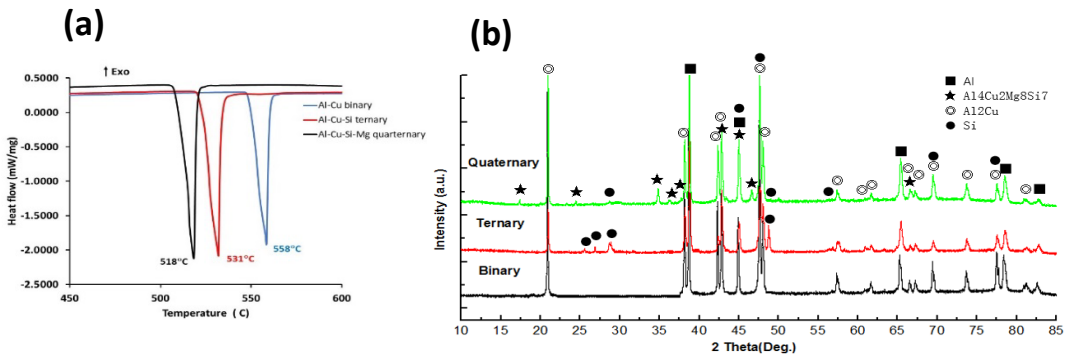

Figure 2 DSC traces (a) and XRD spectra (b) of suction cast $Al_{84}Cu_{16}$(binary), $Al_{81}Cu_{12}Si_7$(ternary) and $Al_{76}Cu_{14}Si_7Mg_3$(quaternary) alloys.

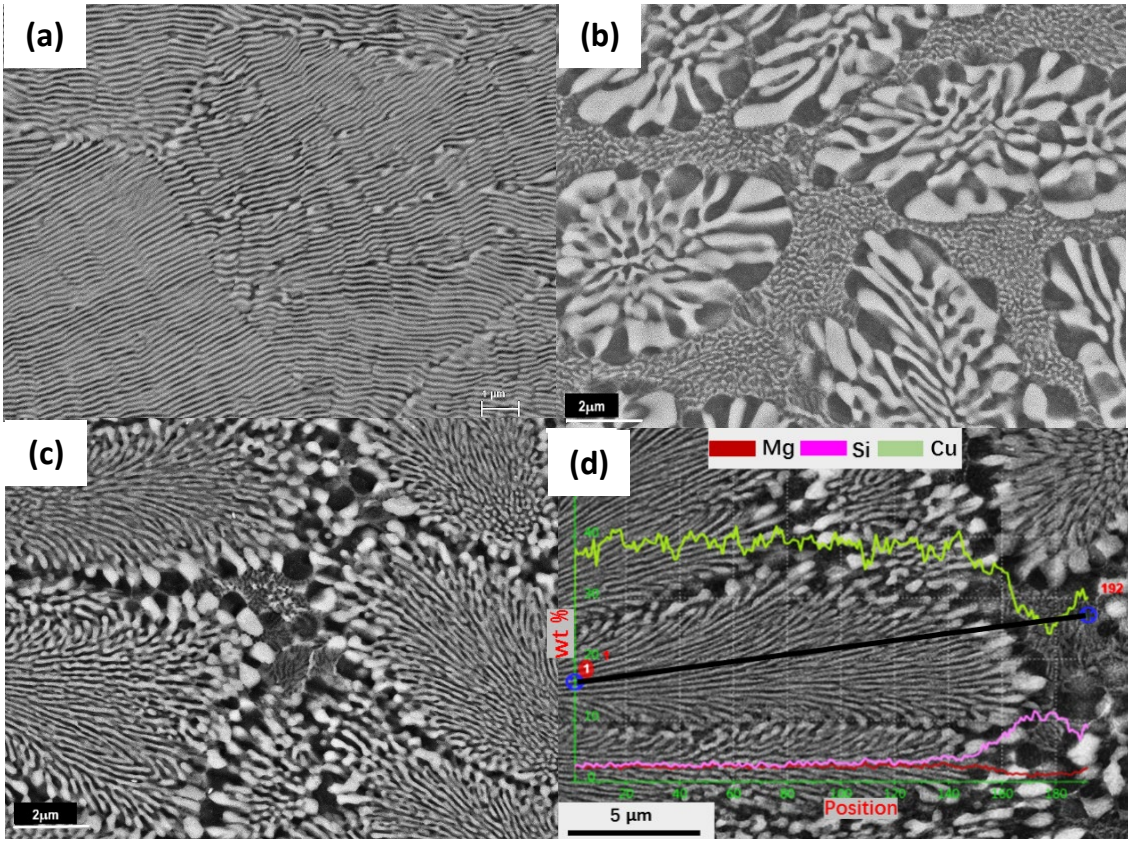

Figure 3 SEM micrographs of suction cast $Al_{84}Cu_{16}$ (a), $Al_{81}Cu_{12}Si_7$ (b) and $Al_{76}Cu_{14}Si_7Mg_3$ (c-d) alloys.

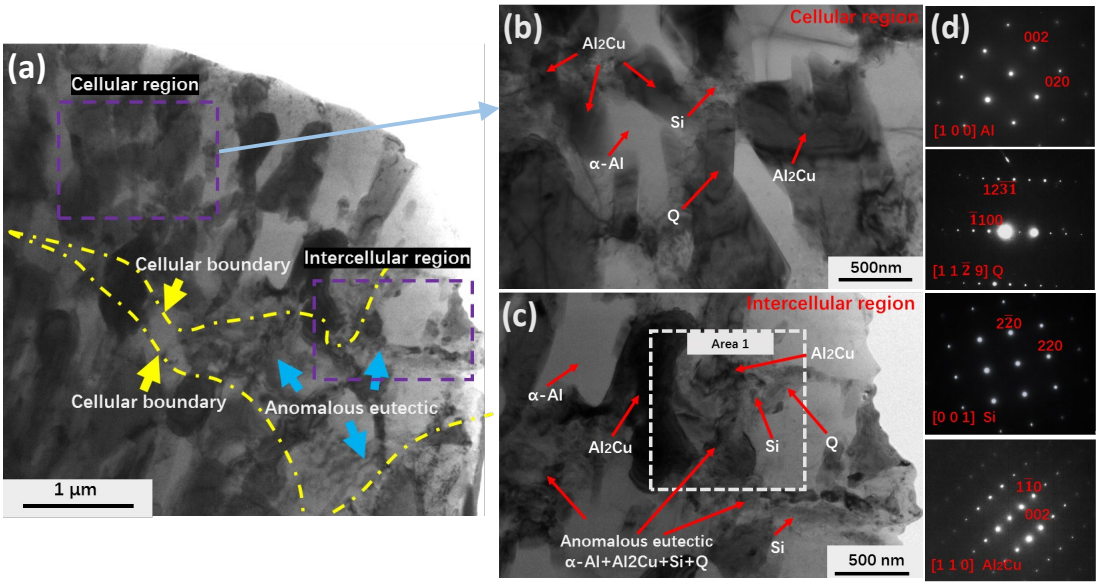

Figure 4 TEM bright-field micrographs of $Al_{76}Cu_{14}Si_7Mg_3$: (a) cellular and intercellular regions; (b) cellular eutectic region with corresponding (c) intercellular region and (d) SADPs of eutectic phases .

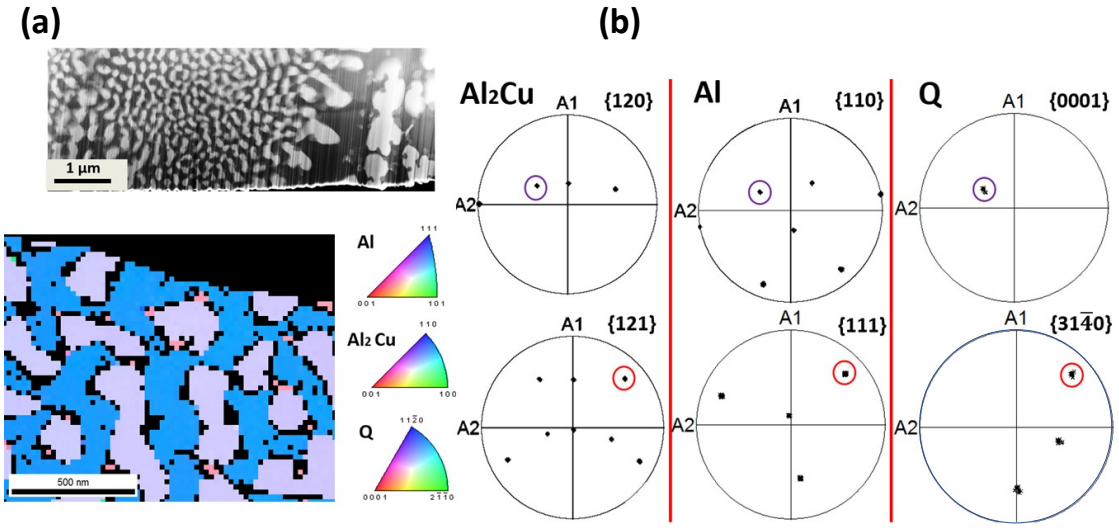

Figure 5 T-EBSD and inverse pole figure map of suction cast $Al_{76}Cu_{14}Si_7Mg_3$ (a) and identification of the orientation relationship between eutectic α-Al, θ-Al_2Cu and Q phases present in the centre of cellular region (b).

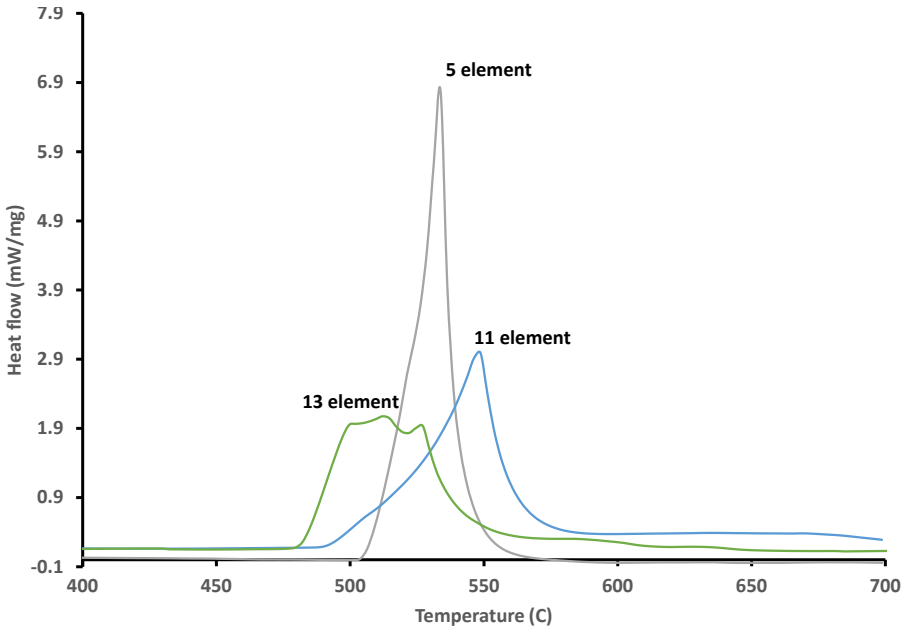

Figure 6 DSC traces of 5-, 11- and 13-element multicomponent alloys obtained from heating at a rate of 20K/min.

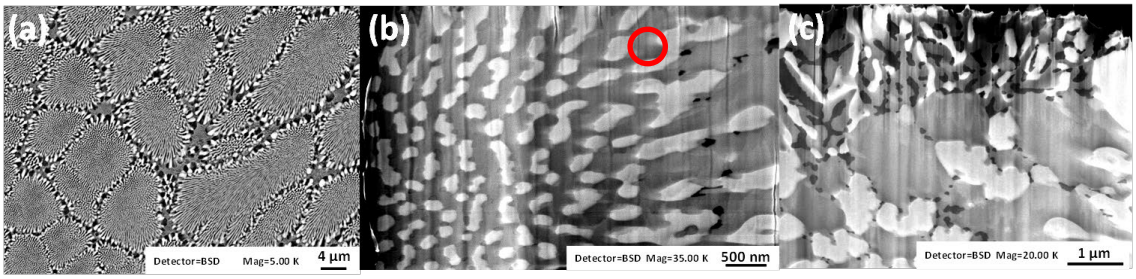

Figure 7 SEM micrograph of cellular eutectic microstructure in suction cast quinary $Al_{77}Cu_{13}Si_6Mg_3Ni_1$ alloy (a), together with FIB-SEM micrographs of the cell (b) and cellular boundary (c) regions taken using the in-lens detector.

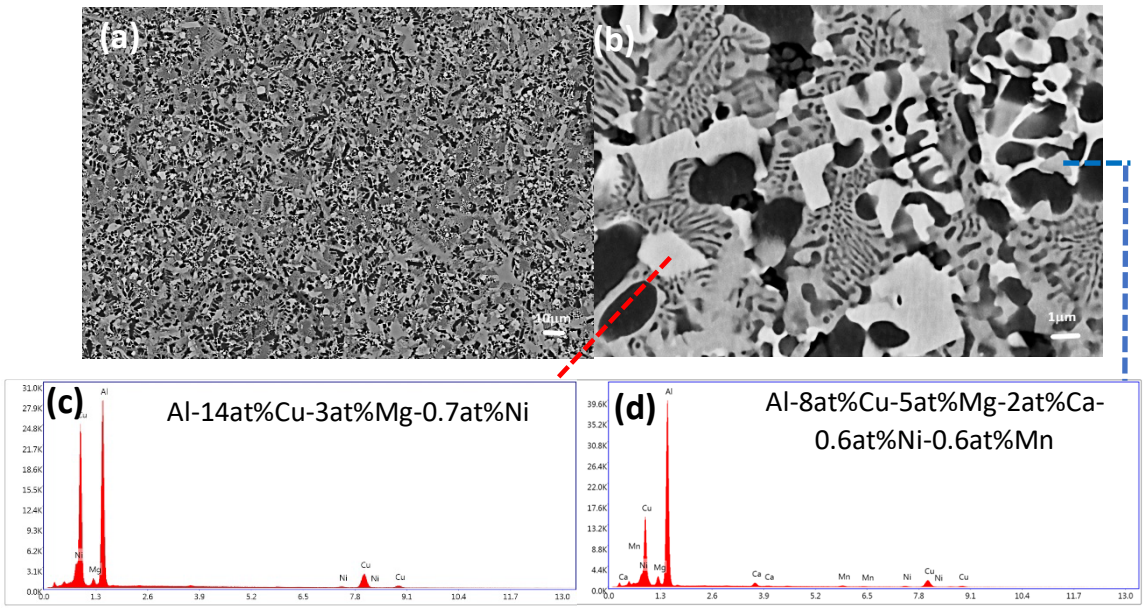

Figure 8 BSE-SEM micrographs of 11-element multicomponent alloy taken at low magnification (a) and high magnification (b) together with EDX spectra of white (c) and grey (d) regions.

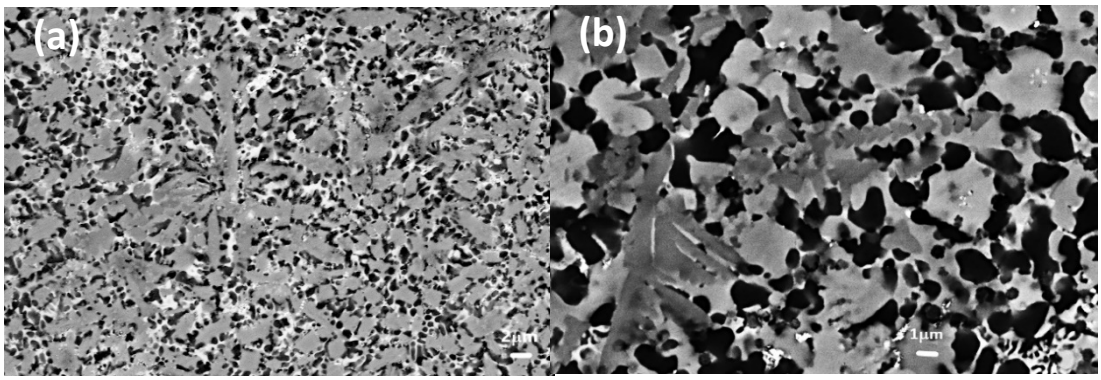

Figure 9 BSE-SEM micrographs of 13-element multicomponent alloy taken as low magnification (a) and high magnification (b).

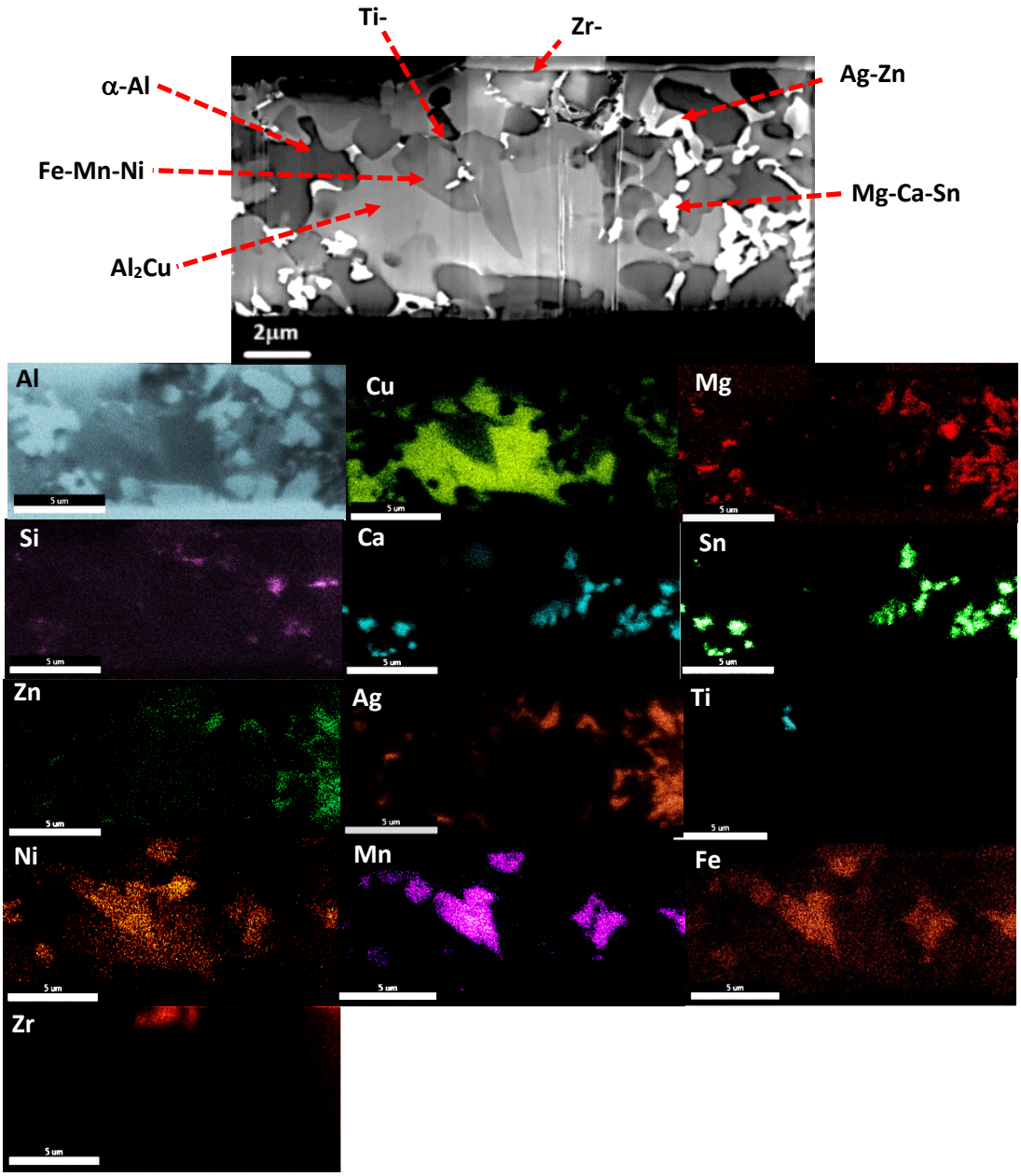

Figure 10 FIB-SEM micrograph of Al $_{72}Cu_{17}Si_{0.9}Mg_{3.8}Ca_{0.7}Fe_{0.2}Mn_{0.7}Ni_{0.9}Ti_{0.4}Zr_{0.1}Ag_{1.6}Sn_{0.7}Zn_1$ alloy, together with X-ray maps showing the corresponding element within each phase.

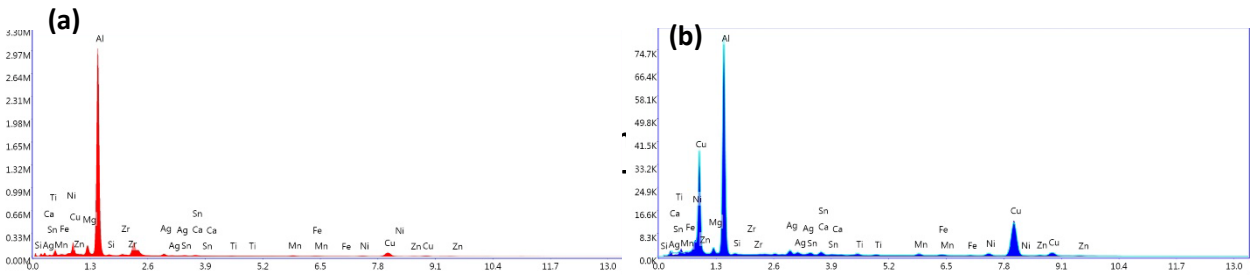

Figure 11 EDX spectra of Al-rich (a) and Cu-containing phases in Al $_{72}Cu_{17}Si_{0.9}Mg_{3.8}Ca_{0.7}Fe_{0.2}Mn_{0.7}Ni_{0.9}Ti_{0.4}Zr_{0.1}Ag_{1.6}Sn_{0.7}Zn_1$ alloy

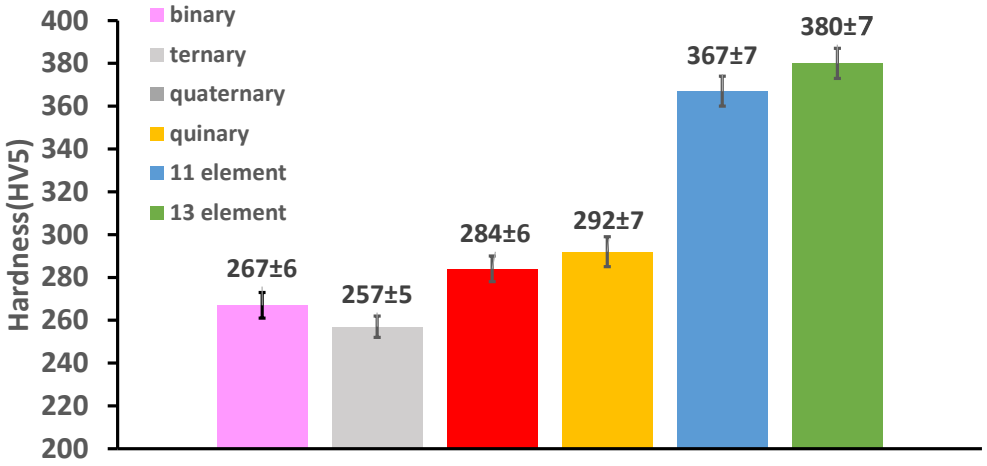

Figure 12 A plot of average Vickers Hardness of suction cast alloys from binary to 13-element multicomponent systems.

Table 1 A selected range of studied eutectic alloys from low to high order constituent systems

Alloy	Phases	References
Binary		
$Al_{84}Cu_{16}$	α-Al+ Al_2Cu	[9 10]
$Al_{61}Ag_{39}$	α-Al +	[11]
$Al_{96.9}Ni_{3.1}$	α-Al + Al3Ni	[9]
$Co_{90.5}Zr_{9.5}$	HCP Co + $Co_{11}Zr_2$	[12]
$Fe_{83}B_{17}$ (annealed)	α-Fe + Fe_2B	[13]
$Fe_{90.2}Zr_{9.8}$	BCC Fe + $Fe_{23}Zr_6$	[12]
$Fe_{90}Nb_{10}$	α-Fe+Fe_2Nb	[14]
$Ni_{80}Si_{20}$	δ-Ni_2Si + γ-$Ni_{31}Si_{12}$	[15]
$Ni_{55}Si_{45}$	γ-$Ni_{31}Si_{12}$ + NiSi	[15]
$Ni_{70}Si_{30}$	δ-Ni_2Si + γ-$Ni_{31}Si_{12}$	[15]
$Ni_{45}Si_{55}$	α-$NiSi_2$ + NiSi	[15]
$Ti_{70.5}Fe_{29.5}$	β-Ti + TiFe	[16]
Ternary		
$Al_{76.07}Cu_{13.6}$ $Ag_{10.27}$	α-Al +θ-Al_2Cu + δ-$AlAg_2$	[43]
$Al_{64.6}Mg_{34.6}Ni_{0.8}$	α-Al + $NiAl_3$ + Mg_2Al_3	[44]
$Al_{81}Cu_{13}Si_6$	α-Al+ θ-Al_2Cu+Si	[41,19,42]

$Co_{49.2}Fe_{49.2}Zr_{9.6}$	BCC Co(Fe) + $Co(Fe_{23}Zr_6)$	12
$Fe_{83}B_{16}Si_1$	α-Fe(Si) +Fe_3B +Fe_2B	49
$Fe_{83}B_{16}Cu_1$	α-Fe(Cu) +Fe_3B +Fe_2B	49
$Fe_{75}Si_{15}Ti_{10}$	α-Fe(Si) + $(Fe,Si)_2Ti$	23
$Fe_{87}Ti_7Zr_6$	α-Fe +Fe_2Ti	24
$Ti_{67.79}Fe_{28.36}Sn_{3.85}$	β-Ti + FeTi	2122
Quaternary		
$Al_{77}Cu_{12}Si_7Mg_3$	α-Al + θ-Al_2Cu + Si + $Q(Al_4Cu_2Mg_8Si_7)$	50
$CoCrFeNi_{2.1}$	FCC + B2	28
$Fe_{71}Si1_5Ti_{10}Cu_4$	α-Fe(Si) + $(Fe,Si)_2Ti$	23
$Fe_{81}Ti_7Zr_6B_6$	α-Fe +Fe_2Ti	24
$Nb_{25}Sc_{25}Ti_{25}Zr_{25}$	HCP + BCC	29
$CrFeNi_2Al_{0.8}$	FCC + B2/BCC	30
Quinary		
$AlCrFeNiMo_{0.2}$	FeCr type solid solution + AlNi intermetallic compound	31
$AlCoCrFeNi_3$	B2 + FCC ($L1_2$)	27
$AlCo_2CrFeNi_2$	B2+FCC ($L1_2$)	27
$Fe_{28.2}Ni_{18.8}Mn_{32.9}Al_{14.1}Cr_6$	FeMn + NiAl	38
$CoCrFeNiMo_{0.8}$	FCC + $Cr_9Mo_{21}Ni_{20}$	32
$CoFeNi_{1.4}VMo$	FCC + Co_2Mo_3	33

$CoFeNi_2V_{0.5}Nb_{0.75}$	FCC +Fe_2Nb type Laves	[34]
$CoCrFeNiZr_{0.45}$	γ-Fe FCC + $ZrCo_2$ type Laves	[35]
$Co_2Mo_{0.6}Ni_2VW_{0.8}$	FCC + Co_7Mo_6-type μ phase	[36]
$Hf_{0.55}CoCrFeNi_2$	FCC + Ni_7Hf_2	[37]
$Ta_{0.65}CoCrFeNi_2$	FCC + $(Co,Ni)_2Ta$	[37]
$Zr_{0.6}CoCrFeNi_2$	FCC + Ni_7Zr_2	[37]
Senary		
CoCrFeNiMnPd	CoCrFeNi + Mn_7Pd_9	[39]
$AlCoCrFeNiNb_{0.6}$	(CoCr)Nb + BCC	[40]

Table 2 A list of multicomponent alloys studied

Number of components	**Alloy composition (at.%)**
5	$Al_{77}Cu_{13}Si_6Mg_3Ni_1$
11	$Al_{70.5}Cu_{18}Si_{0.9}Mg_6Ca_{0.9}Fe_{0.2}Mn_{0.5}Ni_{0.8}Ti_{0.5}Zr_{0.1}Zn_{1.6}$
13	$Al_{72}Cu_{17}Si_{0.9}Mg_{3.8}Ca_{0.7}Fe_{0.2}Mn_{0.7}Ni_{0.9}Ti_{0.4}Zr_{0.1}Ag_{1.6}Sn_{0.7}Zn_1$